Strain sequence effect on fatigue life and fracture surface topography of 7075-T651 aluminium alloy

Wojciech Macek [a,*], Ricardo Branco [b], José Domingos Costa [b], Cândida Pereira [c]

[a] *Gdańsk University of Technology, Faculty of Mechanical and Ocean Engineering, 11/12 Gabriela Narutowicza, Gdańsk, 80-233, Poland*
[b] *University of Coimbra, CEMMPRE, Department of Mechanical Engineering, 3030-788, Coimbra, Portugal*
[c] *Centre for Rapid and Sustainable Product Development, Polytechnic Institute of Leiria, Rua de Portugal, Marinha Grande, 2430-028, Portugal*

ARTICLE INFO

ABSTRACT

The paper studies the effect of strain-loading sequence on fatigue lifetime and fracture surface topographies in 7075-T651 aluminum alloy specimens. Fatigue tests were performed in two ways: (i) constant-amplitude loading and (ii) two series of variable amplitude loading with non-zero mean strain values. The topography of the fatigue fractures was measured over their entire surfaces with the help of an optical confocal measurement system. The results of fatigue tests in the form of equivalent strains, ε_{aeq}, such as the weighted mean of strain components, ε_{a1}, ε_{a2}, and fatigue life, N_f, were used as the sum of the partial number of cycles N_1, and N_2. This study indicates, inter alia, that the values of the fracture surface parameter core height Sk, found in the two-step loading program, are linearly dependent on the equivalent strain, and logarithmically dependent on the fatigue life.

1. Introduction

Aluminium alloys are widely used in many applications due to their good strength-to-weight ratio and corrosion resistance, which results from the formation of a passive oxide layer on the surface (Baragetti et al., 2020; Branco et al., 2019; Carpinteri et al., 2008; Pejkowski and Skibicki, 2019; Rozumek and Faszynka, 2020; Tomczyk and Seweryn, 2017). Nevertheless, pure aluminium has poor monotonic properties, e. g. ultimate tensile strength and yield strength values are about 45 MPa and 17 MPa (Moutarlier et al., 2020). However, for the 7075-T651 aluminium alloy, these values rise to 561 MPa and 501 MPa, respectively (Cunha et al., 2021). Moreover, the 7075-T651 aluminium alloy exhibits better strength relative to the other wrought alloys, but is rather sensitive to pitting, crevices, and the marine environment (Baragetti and Arcieri, 2020; Pandey et al., 2017; Srinivasan et al., 2018; Żebrowski et al., 2019).

Investigations into fracture mechanisms are pivotal to develop reliable engineering components. The analysis of fracture surfaces often demonstrate the presence of cracks which makes the material susceptible to fatigue crack propagation (Branco et al., 2021; Milner and Hutchens, 2021; Pawliczek and Rozumek, 2020). Various methods have been employed to study crack propagation during the material fatigue process, as well as after damage. Numerous mechanisms of crack

nucleation and propagation have been described in aluminium alloys and other metallic materials. Such mechanisms include those based on trimodal microstructure interactions (Tan et al., 2020) or the development of micro-cracks mainly at grain boundaries (GB) and triple junctions (Madivala et al., 2019). Zhang et al. (2020) have made successful attempts to find a ductile fracture criterion. Their criterion can accurately predict the onset of ductile fracture for Al6016-T4 in the medium stress triaxiality. Ductile fracture criteria in the macro-forming domain has been investigated by Ran and Fu (2016). The results of their simulations were compared to those of an experiment to determine the most suitable criterion for flanged upsetting and extrusion processes. Also, many observation techniques, including optical microscope (OM), scanning electron microscope (SEM), energy dispersive spectrometer (EDS), and finite difference method (FDM) have been used to investigate processes such as the hot tears mechanisms in the cast AC4BAl engine (Yu et al., 2021). In addition, there has been a lot of work on predicting the fatigue crack growth (FCG) rates numerically (Borges et al., 2020; Vukelic and Brnic, 2016).

The morphology of the material can be examined within the material (Fisher and Marquis, 2016; Hebda et al., 2020; Wang et al., 2019) and on its surface (Kida et al., 2017; Lauschmann and Šiška, 2012; Macek et al., 2020c). Xu et al. (2021) conducted fractographic examination to account for the influence of shear impact loading. They identified different

---

Table 1

Monotonic mechanical properties of the 7075-T651 aluminium alloy [5].

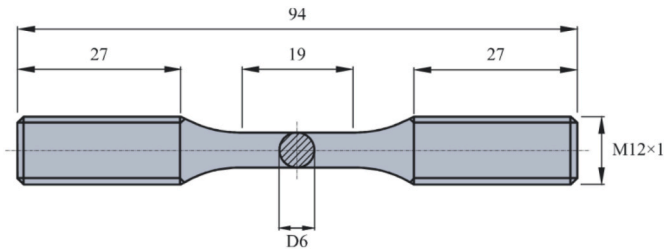|	
Yield strength (MPa)	501
Ultimate tensile strength (MPa)	561
Young's Modulus (GPa)	71.7
Elongation (%)	9.7
Reduction in area (%)	29.1

Fig. 1. Specimen geometry used in low-cycle fatigue campaign (units: mm).

fracture mechanisms, depending on the rate of loading. The failure revealed a brittle-ductile mixed-mode fracture mode under quasi-static conditions. Three-dimensional surface profilometry has also been used to study the tribological response of SiC fracture surfaces (Huang and Feng, 2006). In addition, a dynamic friction model with overstress and relaxation has been developed. Post-failure techniques measuring fracture surface parameters after common fatigue tests, or even for service loads with strain-load sequences, may have potential to estimate the lifetime and must be experimentally validated (Cisko et al., 2019). In some works, scientists have tried to combine different methods, linking them to fracture mechanisms or fatigue life, especially using surface roughness values evaluated along the fractures surface areas (Macek et al., 2020; Pomberger et al., 2020; Sampath et al., 2018; Slámečka et al., 2010) and considering different uniaxial and multiaxial loading conditions (Macek, 2019a, 2019b; Macek et al., 2021; Macek et al., 2020a, 2020b). Therefore, in this paper, we attempt to link the fracture surface topography parameters with the fatigue loading conditions under variable amplitude. Surface analysis was performed on the entire fracture area, without partition into regions of initiation and propagation. Verification of the influence of the strain sequence on the fracture surface texture was carried out and described with core height, Sk, which represents the height of the core surface. Sk parameter is a value obtained by subtracting the minimum height from the maximum height of the core surface.

This paper starts with the study of fatigue behaviour of 7075-T651 aluminium alloy specimens under constant-amplitude and two-step fatigue loading. Then, the fracture surface topography is analysed using a three-dimensional optical confocal scanning microscope. Fracture topography measurements are carried out using the entire fracture area

method. After that, the effect of fatigue loading sequences on the fracture surfaces, in connection with the fracture surface topography measurements associated with the tested fatigue scenarios are investigated.

Following the Introduction, the paper is organised as follows: Section 2 describes the materials and methods used for this research. Section 3 gathers information on the experimental fatigue and fracture surface program. Section 4 presents the main outcomes of the fatigue campaign and the fracture surface parameters. The paper ends with a summary of the most relevant findings. Finally, appendixes A and B show the 3D view, photo simulation, Sk and volume parameters, as well as a comparison of both sides of the specimen.

2. Materials and methods

2.1. Fatigue testing campaign

Fatigue experimental results were taken from the paper presented by Cunha et al. (2021). The specimens used in this research were made from a 7075-T651 aluminium alloy supplied in the from a 20 mm thick plate. The main monotonic mechanical properties of the tested alloy are listed in Table 1. The specimens geometries, schematised in Fig. 1, were manufactured according to the ASTM E−647 standard and had a gauge section with a length of 19 mm and a diameter of 6 mm. Stress-strain data were recorded using a 12.5 mm long gauge extensometer clamped directly to the specimen via two separated knife-edges. Tests stopped when total failure has occurred.

Fatigue tests were performed under uniaxial strain-controlled conditions using sinusoidal wave forms and a constant strain rate ($d\epsilon/dt = 8 \times 10^{-3}$ s^{-1}). The loading scenarios comprised: (i) constant-amplitude and (ii) two-step loading histories. Regarding the former case, see Fig. 2(a), the tests were conducted under fully-reversed conditions ($R_\epsilon = -1$) with a constant strain amplitude (ϵ_a). Concerning the latter, two loading sequences were studied, namely a symmetrical-asymmetrical sequence and an asymmetrical-symmetrical sequence. The symmetrical-asymmetrical sequence (see Fig. 2(b)) consisted of an initial step with a strain amplitude $\epsilon_{a,1}$ applied under fully-reversed conditions ($R_{\epsilon,1} = -1$) followed by a second step with a positive mean strain ($R_{\epsilon,2} = -1$) and a strain amplitude $\epsilon_{a,2}$. The asymmetrical-symmetrical sequence (see Fig. 2(c)) consisted of a first step with a

Table 2

Summary of low-cycle fatigue testing campaign (Cunha et al., 2021).

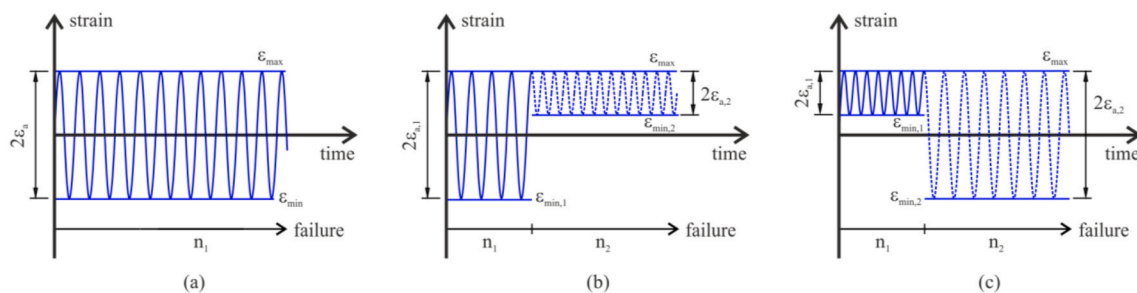| Test	1	2	3	7	9	14	15
$\epsilon_{a,1}$ (%)	1.25	1.00	0.50	1.25	1.00	0.50	0.50
$\epsilon_{a,2}$ (%)	–	–	–	0.50	0.50	1.25	1.00
$R_{\epsilon,1}$	−1	−1	−1	−1	−1	0.20	0
$R_{\epsilon,2}$	–	–	–	0.20	0	−1	−1
N_1 (cycle)	167	302	11084	33	68	2216	2216
N_2 (cycle)	–	–	–	2092	3719	26	319
N_f (cycle)	167	302	11084	2125	3787	2242	2535

Fig. 2. Outline of loading sequences followed in low-cycle fatigue tests: (a) fully-reversed constant-amplitude loading ($R_\epsilon = -1$), (b) symmetrical-asymmetrical sequence ($R_{\epsilon,1} = -1$, $R_{\epsilon,2} = 1 - (2\epsilon_{a,2}/\epsilon_{a,1})$, and c) asymmetrical-symmetrical sequence ($R_{\epsilon,1} = 1 - (2\epsilon_{a,1}/\epsilon_{a,2})$, $R_{\epsilon,2} = -1$). R_ϵ represents the stain ration and is defined by $\epsilon_{min}/\epsilon_{max}$.
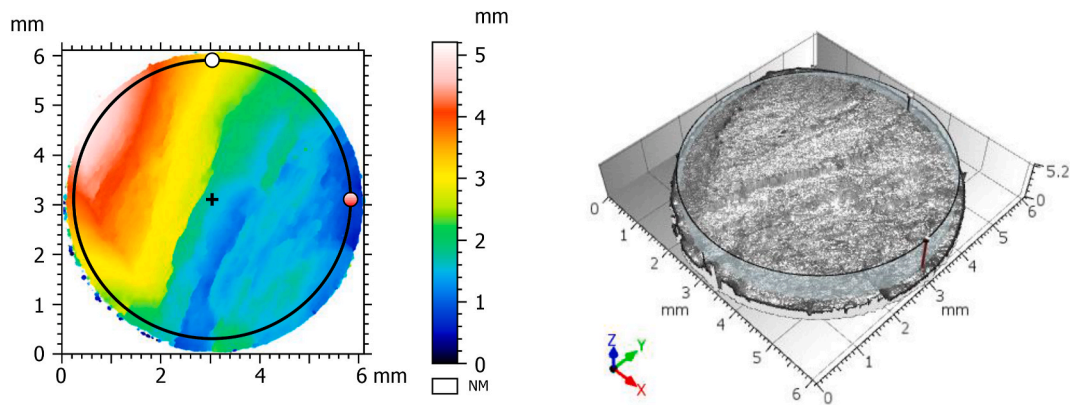
Fig. 3. Original and marked final surfaces in pseudo-color and grey views for specimen 15 (side B). (For interpretation of the references to color in this figure legend, the reader is referred to the Web version of this article.)
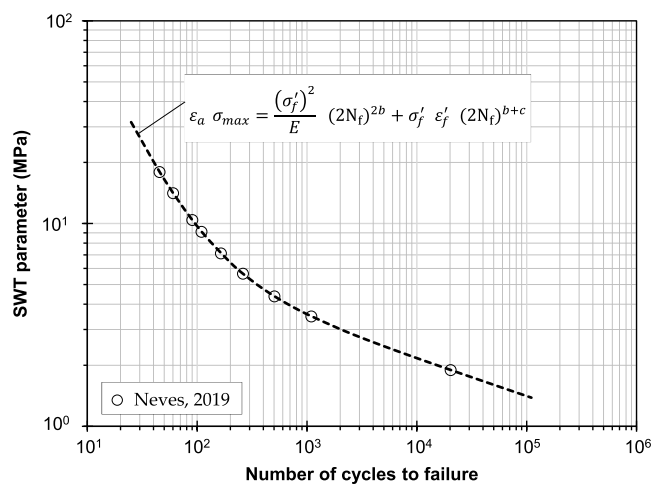

Fig. 4. SWT damage parameter versus number of reversals to failure (N_f). Strain amplitude and maximum stress were computed from the fully-reversed strain-controlled tests using the half-life cycle (Neves, 2019).

The displayed equation:

$$\varepsilon_a \ \sigma_{max} = \frac{(\sigma_f')^2}{E} \ (2N_f)^{2b} + \sigma_f' \ \varepsilon_f' \ (2N_f)^{b+c}$$

positive mean strain ($R_{\epsilon,1} = -1$) of strain amplitude $\epsilon_{a,1}$ followed by a second step with a strain amplitude $\epsilon_{a,2}$ applied under fully-reversed conditions ($R_{\epsilon,2} = -1$). The first step of the loading sequence tests was applied for a limited number of cycles (N_1) defined as 20% of the total fatigue life (N_f) of the constant-amplitude case carried out at the same

strain amplitude. Table 2 provides a summary of the strain amplitudes and strain ratios considered in this research.

2.2. Fracture surface measurement

Measurements of the surface topography were made using a Leica DCM8 non-contact 3D optical surface metrology system, equipped with a confocal microscopy unity as well as interferometry and optical pro-filometry units. The latest evolution is an all-in-one versatile system that provides fast 3D surface measurement solutions for metrology observation tasks (Tsigarida et al., 2021). All measurements were made using a 5× lens, using the Focus Variation technique with an increased speed factor, therefore the measurement time was significantly reduced. It is designed to complement confocal measurements at low magnification. However, the focus variation acquires topographies in a wide field mode, which means that the complete field of view on the sample surface is illuminated. Due to the restricted field of view (FOV), more precisely 3508 × 2640 μm, pictures were stitched together to map the entire fracture area. Each individual micrograph had a vertical resolution of <150 nm with an optical resolution of 0.94 μm. The numerical aperture for 5× objective magnification was 0.15.

For the entire fracture area method, measurements on other 3D optical profilers (Alicona IF G4 and Sensofar S neox) with different magnifications (e.g. 10×, 5×) were also tested and it was concluded that parameters such as points density have a negligible impact on the surface topography measurements.

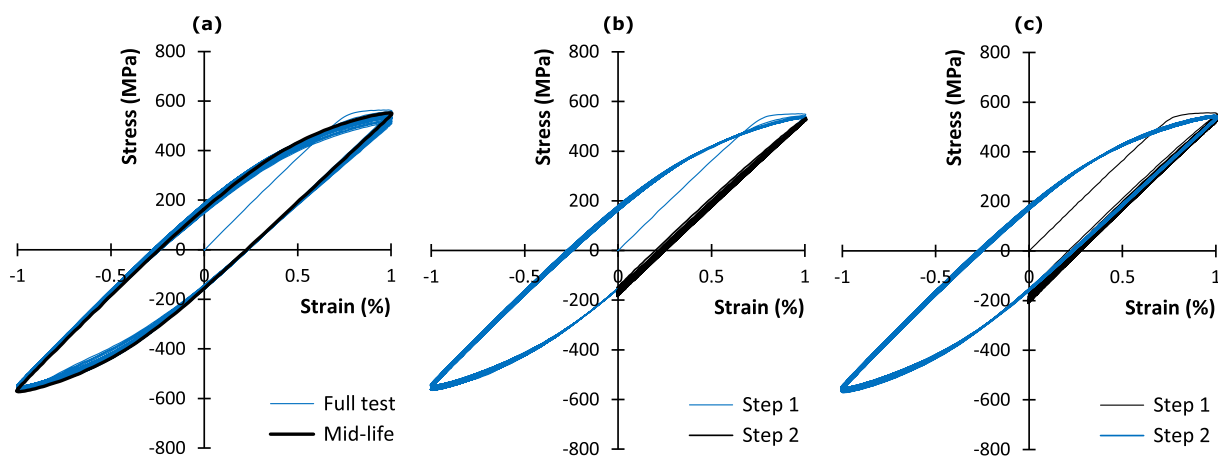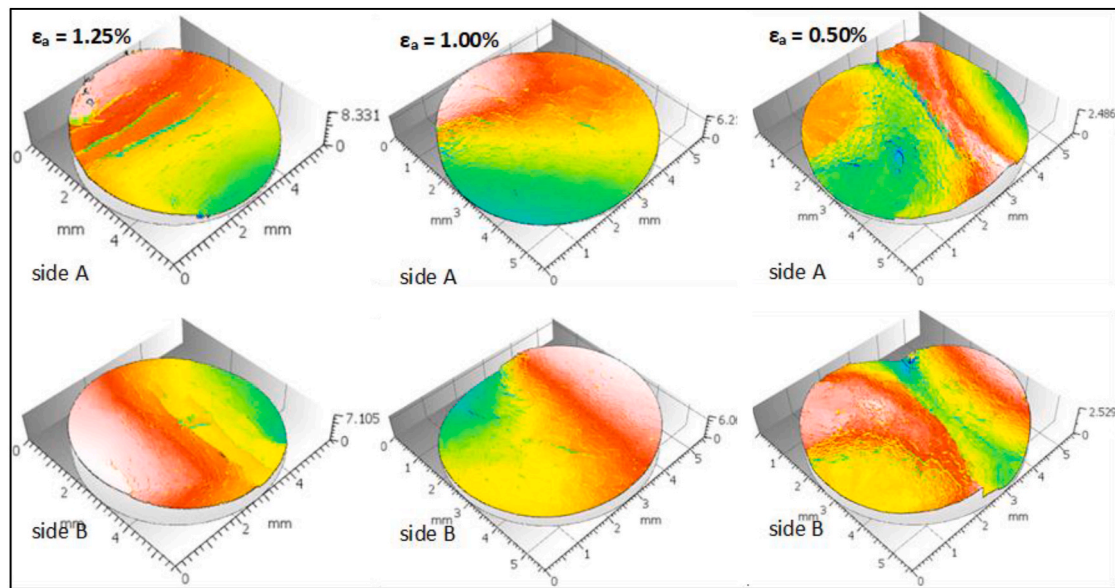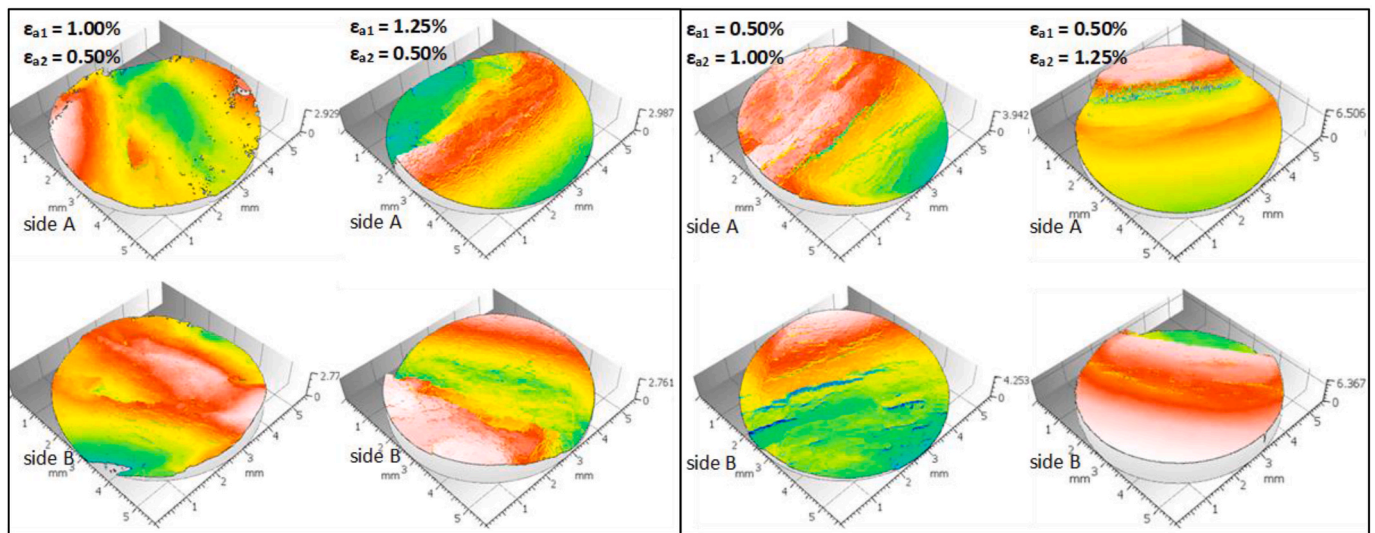After measurements, Leica (*.plux) files were imported into the

Fig. 5. Cyclic stress-strain response registered in the strain-controlled fatigue tests: (a) fully-reversed constant-amplitude loading with $\varepsilon_a = 1.00\%$, (b) symmetrical-asymmetrical loading sequence ($\varepsilon_{a,1} = 1.00\%$, $\varepsilon_{a,2} = 0.50\%$), (c) asymmetrical-symmetrical loading sequence ($\varepsilon_{a,1} = 0.50\%$, $\varepsilon_{a,2} = 1.00\%$).

(a)

(b)   (c)

Fig. 6. Extracted fracture areas for: (a) fully-reversed constant-amplitude loading, (b) symmetrical-asymmetrical loading sequences, and (c) asymmetrical-symmetrical loading sequences.

MountainsMap surface metrology software and resampled into height maps at a resolution automatically determined by the software. Surfaces were analysed in relative coordinates (X, Y, and Z axes), with the Z axis in heights from the lowest point by default. No additional filters were used. Fatigue fracture surfaces were measured for total areas and both sides of the fracture surface, termed here side A and side B. Additionally, the whole current surface was reduced to a circle of 5.6 mm diameter to eliminate the final break, discontinuities and "non-sampling" areas. Based on the example of specimen 15 (side B), Fig. 3 shows a selected measuring area marked with a circle.

To check the fracture surface dependency on the fatigue loading scenarios, selected functional parameters, namely the core height (Sk), were selected according to the ISO 25178-2 standard ("ISO - ISO 25178–2:2012 - Geometrical product specifications (GPS) — Surface texture: Areal — Part 2: Terms, definitions and surface texture parameters," n.d.; Todhunter et al., 2017). This functional parameter showed the highest compliance regarding the fatigue parameters. The

parameters carry out a separation of the height distribution represented by the Abbott curve into three parts: (1) related to the peaks (Spk); (2) related to the core area (Sk); and (3) related to the valleys (Svk). A graphical interpretation of the Sk parameters is provided in Figs. A1 and A2 of Appendix A.

2.3. Lifetime and strain analysis

The low-cycle fatigue campaign, as explained above, comprised different loading scenarios. After determining the number of cycles to failure (N_f) for the tests conducted under constant-amplitude loading, the testing program for variable-amplitude loading was designed in such a way that the number of cycles of the first step (N_1) was always 20% of N_f value of the case performed with the same strain amplitude. The second step was applied until total failure has occurred and the associated number of cycles was represented by N_2. Thus, N_f can be defined by Eq. (1).
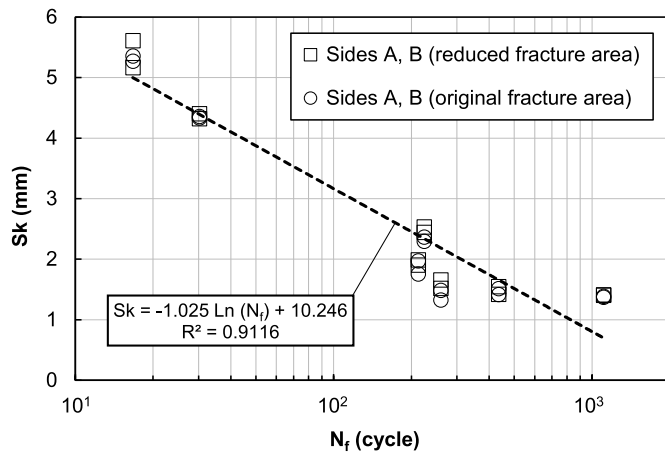
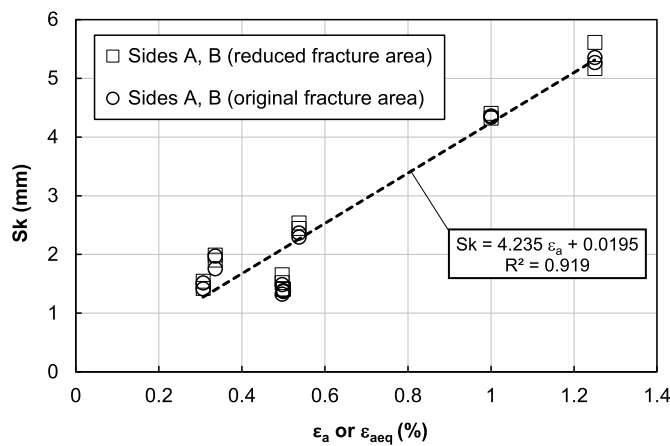**Fig. 7.** Core height, Sk, versus number of cycles to failure, N_f.

Fig. 8. Core height, Sk, versus strain amplitude, ε_a or ε_{aeq}.
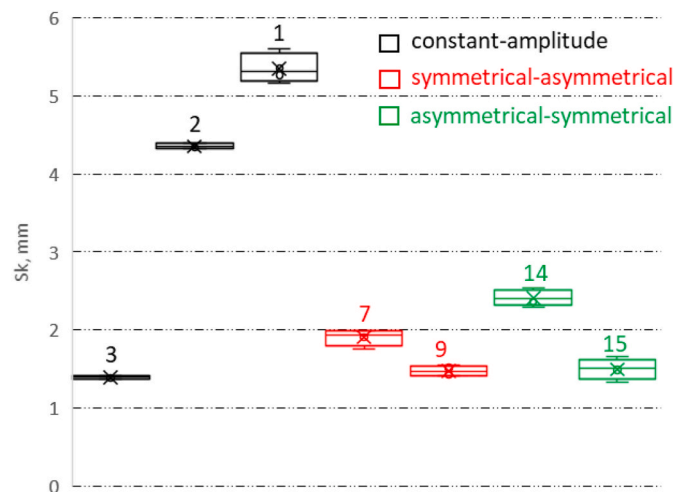

Fig. 9. Comparison of core height, Sk, parameters for fully-reversed constant-amplitude loading, symmetrical-asymmetrical sequences, and asymmetrical-symmetrical sequence.

$$N_f = N_1 + N_2 \qquad (1)$$

For the analysis of the relationship between the strain amplitude and the fracture surface parameters, presented later in this article, the equivalent strain amplitude (ε_{aeq}) is used:

$$\varepsilon_{aeq} = D_1 \cdot \varepsilon_{a,1} + D_2 \cdot \varepsilon_{a,2} \qquad (2)$$

where D_1 and D_2 represent the fatigue damage associated with the steps 1 and 2, respectively; and ϵ_{a1} and ϵ_{a2} are the strain amplitudes of the steps 1 and 2, respectively. In this study, the fatigue damage associated with each step was accounted for using the Miner-Palmgren linear damage rule. For a two-step loading case, it leads to:

$$D = \frac{n_1}{N_1} + \frac{n_2}{N_2} \qquad (3)$$

where n_1 and n_2 are the numbers of cycles applied at the first and second strain levels, respectively; and N_1 and N_2 are the fatigue life at the first and second strain levels. In this study, unlike the classical approaches based on the stress-life relationships, the fatigue at the first (N_1) and second (N_2) strain levels were defined using the Smith-Watson-Topper (SWT) parameter:

$$SWT = \varepsilon_a \cdot \sigma_{max} \qquad (4)$$

where ϵ_a is strain amplitude and σ_{max} is the maximum stress. This fatigue quantifier uses stress and strain terms, which make it more suitable to deformation-sensitive materials. In addition, it is also able to account for mean stress effects occurring in the case of the asymmetrical steps. The SWT parameter versus fatigue life relationship for the 7075-T651 aluminium alloy, determined from fully-reversed strain-controlled conditions, is presented in Fig. 4 (Neves, 2019). As can be seen, the fitted functions are quite close to the experimental points.

3. Results

### 3.1. Low-cycle fatigue results

The fatigue lives obtained in the tests for constant-amplitude and step loading conditions are listed in Table 2. As can be seen in the table, under constant-amplitude fatigue lives diminish as the strain amplitude increases, which agrees with the general trends found in the literature for metals subjected to strain-controlled conditions. In the case of the step loading tests, fatigue lives for tests 8 and 9, which have the same strain amplitudes but applied in opposite sequences, the number of cycles to failure is quite similar. Regarding the tests 10 and 13, although the strain amplitudes are also similar, the loading sequence affected the fatigue life.

Fig. 5 shows some examples of the cyclic stress-strain response registered in the experimental strain-controlled fatigue tests, either under constant-amplitude and two-step loading conditions. As can be seen, under constant-amplitude loading (Fig. 5(a)), the material shows smooth variations of both maximum tensile and maximum compressive stresses in most of the test, since the values of the mid-life cycle are close to those of the initial cycle. At this strain amplitude, a close look at the hysteresis loop shapes shows a strain-softening behaviour, i.e. a decrease of the uncontrolled stress as the number of cycles increases. In a second stage, when the total failure is approaching, this effect becomes more visible, and there is a clear reduction of the maximum tensile stress over time. Regarding the two-step tests, the changes of the hysteresis loops are greater if a loading block is applied during the first stage or the second stage of the test. Comparing the symmetrical-asymmetrical (Fig. 5(b)) and the asymmetrical-symmetrical (Fig. 5(a)) cases, it is clear that the cyclic deformation response depends on the loading sequence, e.g. the strain-softening behaviour of the first step of the asymmetrical-symmetrical test is different from the second step of the symmetrical-asymmetrical test. However, the deformation sensitivity of the tested alloy is not much significant, which can be explained by its face-centred cubic crystal structure with high stacking fault energy (Neves, 2019).

Table 3

Summary of the low-cycle fatigue testing campaign under variable-amplitude loading (Neves, 2019).

Test	4	5	6	7	8	9	10	11	12	13	14	15
$\varepsilon_{a,1}$ (%)	1.50	1.50	1.25	1.25	1.00	1.00	0.70	0.50	0.70	0.70	0.50	0.50
$\varepsilon_{a,2}$ (%)	0.70	0.50	0.70	0.50	0.70	0.50	1.50	1.50	1.25	1.00	1.25	1.00
$\sigma_{max,1}$ (MPa)	580.9	575.0	563.5	556.1	544.1	534.3	540.2	558.7	550.1	524.4	503.4	526.8
$\sigma_{max,2}$ (MPa)	535.6	555.0	559.1	542.1	541.2	517.5	572.2	570.0	560.3	530.7	579.7	547.0
N_1 (cycle)	24	24	33	33	68	68	265	2216	265	265	2216	2216
N_2 (cycle)	861	2893	559	2091	637	3719	117	48	150	267	26	319
N_f (cycle)	885	2917	592	2124	705	3787	382	2264	415	532	2242	2535
N_p (cycle)	668	2190	559	2487	653	3018	343	2234.	372	471	2636	2318
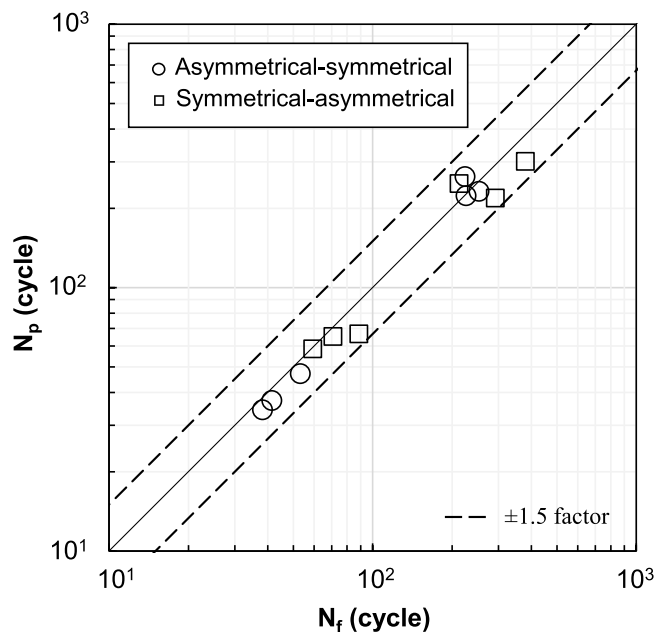
Fig. 10. Experimental fatigue life, N_f, versus predicted fatigue life, N_p, under variable amplitude loading.

3.2. Post-mortem measurement of the crack surface

After the fatigue tests, the fracture surfaces were measured using the non-contact 3D optical surface metrology system. The cases verified in this study showed the greatest compatibility based only on the core height (Sk) parameters of the ISO 25178-2 standard that are associated with the functional characteristics of the element.

Fig. 6 presents extracted fracture areas after low-cycle fatigue testing for (a) fully-reversed constant-amplitude loading (Fig. 6(a)); symmetrical-asymmetrical loading sequences (Fig. 6(b)); and asymmetrical-symmetrical loading sequences (Fig. 6(c)). All 3D surface parameters, as referred to above, were calculated on the entire surface which was reduced to a circle with 5.6 mm diameter, in order to eliminate the final break, discontinuities and "non-sampling" areas.

In the case of the constant-amplitude test, the samples with higher values of strain amplitude (ε_a) had greater Z-axis height differences within the crack surface (see Fig. 6(a)). Regarding the symmetrical-asymmetrical ((Fig. 6(b)) and asymmetrical-symmetrical (Fig. 6(c)) loading sequences applied in the first step ($\varepsilon_{a,1}$) of the variable-amplitude loading tests, the results show that there is no practical effect on the Z-axis height values, i.e. there is no relevant changes. On the contrary, the values of strain amplitude applied in the second step ($\varepsilon_{a,2}$) of the variable-amplitude loading tests had a greater impact on surface topography parameters (Fig. 6(c)).

Another interesting outcome is that both sides of the broken samples showed similar values of the measured surface topography parameters. As far as the maximum values of the surface height are concerned, the greatest difference between the A and B sides occurred for the fully-reversed constant-amplitude sample with strain amplitude $\varepsilon_a = 1.25\%$, reaching 17.3%. Therefore, for most of the surface topography parameters in this type of loading, it does not matter which side of the broken specimen is analysed. Detailed information about the 3D view, photo simulation, core height and volume parameters of the extracted areas for each strain level is presented in Appendix A.

4. Discussion

4.1. Influence of fatigue life N_f and strain components ε_a on the fracture surface

The results of surface topography measurements were analysed in the form of a selected parameter - the core height, Sk - in relation to the number of cycles to failure, N_f, and the strain amplitude, ε_a or ε_{aeq}. The results were obtained for the fracture surfaces before selection of a circle with a diameter of 5.6 mm and after narrowing the measurement area, as well as for both sides (A and B) of the broken samples. For the analysed cases, the core height versus the number of cycles to failure relationship is shown in Fig. 7. Depending on the strain sequences applied, various fatigue fracture results were obtained. The results of the research undertaken in this work indicate a strong influence of the strain sequences applied in the low-cycle fatigue tests on the fracture surface roughness characterised by the core height parameter. The proportion of the variance for a dependent variable, expressed by the R-squared (R^2), is approximately 0.91. It is also clear that the measurements carried out for the original fracture areas and those obtained from the reduced areas are quite similar. On the other hand, there is a reduction of the core height parameter with the increase of the fatigue lifetime.

Regarding the relationship between the core height, Sk, parameter and the equivalent strain amplitude, ε_a or ε_{aeq}, the trend, referring to the examined specimens subjected to different strain loading conditions, are shown in Fig. 8. It can be seen that the core height parameter increases with the strain amplitude. This may be explained by the higher fatigue crack growth rates associated with higher strain levels, causing higher roughness. Overall, there is a good correlation between both variables, which can be fitted by a linear relationship. The proportion of the variance, expressed by the R-squared (R^2), is around 0.92. In addition, similarly to the previous case, the differences associated with the measurements obtained with the original and the reduced areas is not significant.

Comparison of core height, Sk, parameters in the context of fully-reversed constant-amplitude loading as well as symmetrical-asymmetrical and asymmetrical-symmetrical loading sequences is shown in Fig. 9. The boxes are drawn between the first and third quartiles, with additional lines drawn along the second quartile to mark the median. Minimums and maximums outside the first and third quartiles are depicted with whiskers, while mean markers are denoted by x. The width of the boxes shows that the differences between both parts of the broken samples (side A and side B) and for the reduced and total measured areas are negligible. Small differences in the geometry of the fractures of both parts of the samples are confirmed in Appendix B. The validation was made by adjusting the angle of rotation of the sample
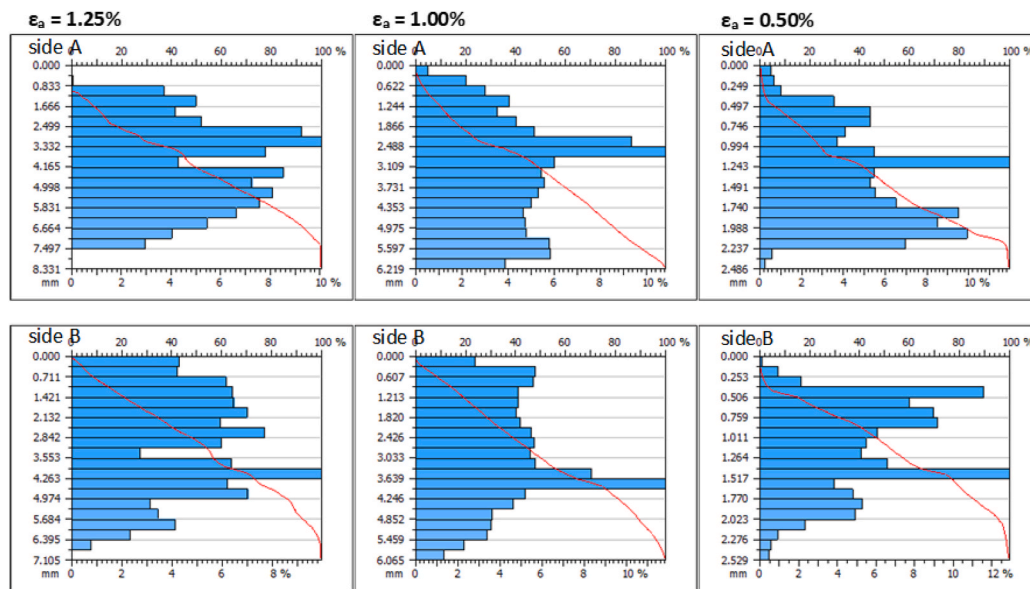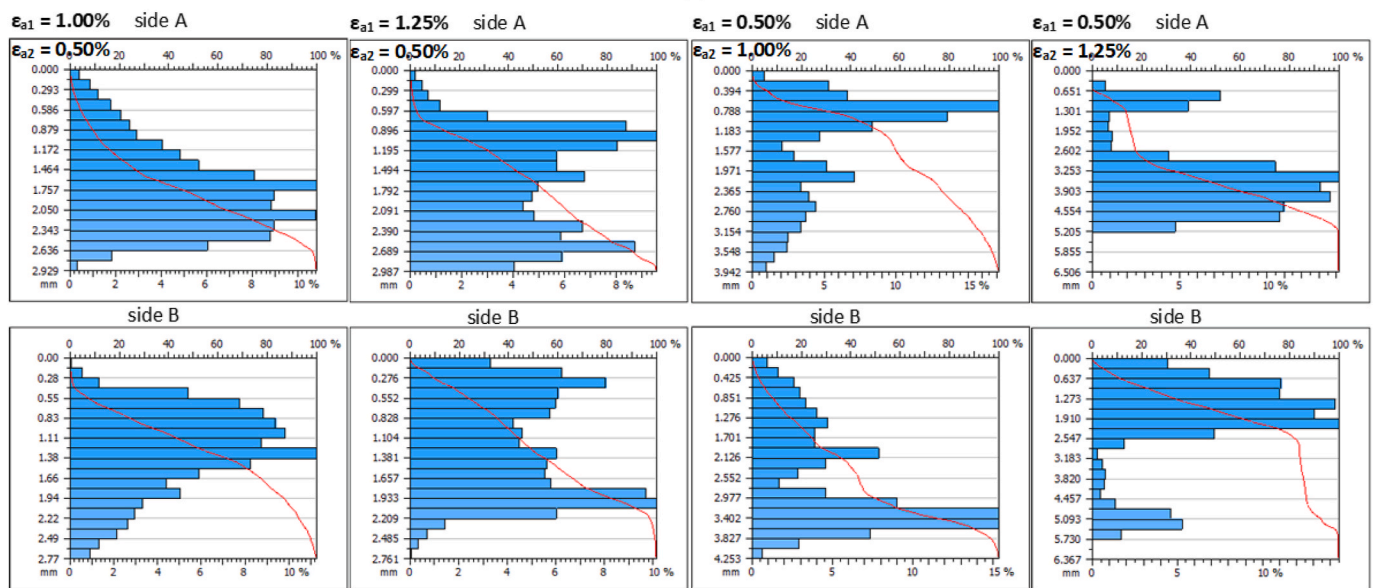
Fig. 11. Abbott-Firestone plots for: (a) fully-reversed constant-amplitude loading, (b) symmetrical-asymmetrical loading sequence, and (c) asymmetrical-symmetrical loading sequence (cases of Table 2). The horizontal axis represents the bearing ratio (%), and the vertical axis represents the depths (milimeters).

in the Z axis and then mirroring it. The surfaces prepared in this way, together with the measurement results, can also be used for further comparative analyses focused on the cracking mechanisms. Such analyses may be carried by using, for example, the FRASTA method (Kobayashi and Shockey, 2010; Sampath et al., 2018) but this approach is not the subject of this paper. In the present paper, for further fracture surface topography analyses, the entire fracture method based on the reduced area will be used, due to the reduction of the unmeasured points near the fracture edge.

4.2. Evaluation of fatigue life under variable amplitude loading

In order to test the predictive capabilities of the proposed fatigue life assessment method, additional low-cycle fatigue tests under variable-amplitude loading (i.e. symmetrical-asymmetrical and asymmetrical-symmetrical sequences) were taken into account (Neves, 2019).

Table 3 listed the cases presented in Table 2 for variable amplitude loading and well as the new cases. Fatigue life predictions were performed using the SWT damage parameter in conjunction with the Miner-Palgren linear damage rule (see Section 2.3). The maximum stress values obtained in the experiments for the half-life cycle of the first step loading ($\sigma_{\max,1}$) and the second step ($\sigma_{\max,2}$) loading as well as the predicted fatigue life (N_p) are compiled in Table 3. Fig. 10 plots the predicted fatigue life (N_p) against the experimental fatigue life (N_f) for the different loading cases. For the sake of comparability, factor bands with factors of 1.5 were plotted. It is worth to note that the predictions based on the proposed approach fall within a narrow range, which is an interesting outcome. In addition, the predictions are slightly conservative, which is also another positive aspect. Overall, these results clearly demonstrate that the SWT damage parameter combined with the Miner-Palgren rule can appropriately capture the effect of load sequence on fatigue behaviour of the 7075-T651 aluminium alloy under two-step

loading.

4.3. Distribution of fracture surface heights in the loading sequences context

Fig. 11 shows the Abbott-Firestone plots for the fully-reversed constant-amplitude loading, symmetrical-asymmetrical loading sequence, and asymmetrical-symmetrical loading sequence (cases of Table 2). This type of plot, which relates the distribution of heights and the cumulated curve, is one of the surface characterization techniques that best represent the functional characteristics of the surface. Therefore, it can provide important information on the surface properties in a systematic and quantitative approach.

The Abbott-Firestone plots show the bearing ratio curve and depth distribution histogram (see Fig. 11). In general, for the Abbott-Firestone plot, the minimum values of the Sk in all cases tested demonstrate that the histogram distribution is more even. This is manifested by the fact that the largest measured Sk values ($\varepsilon_a = 1.25\%$ and $\varepsilon_{a1} = 1.25\%$) have the lowest depth distribution values (about 10%). On the other hand, the lowest Sk values, occurring for $\varepsilon_a = 0.50\%$ and $\varepsilon_{a1} = 0.50\%$, generate the highest percentages, approximately equal to 12% and 15%, respectively.

On the Abbott-Firestone plots, the cases with the smallest strain amplitude under fully-reversed constant-amplitude (ε_a) and smallest strain amplitude in the second step under symmetrical-asymmetrical loading (ε_{a2}) are characterised by the smallest values of height distribution. Comparing the plots for both sides of the sample break (side A and side B), they show a mirror image, and the differences are not significant.

5. Conclusions

In this study, fracture surface properties of 7075-T651 aluminium alloy specimens under constant- and variable-amplitude loading under strain-controlled conditions were investigated. The triangular relationship between: (1) the strain sequence for both symmetrical-asymmetrical and asymmetrical-symmetrical conditions; (2) the surface topography parameters in the form of core height, Sk, measured using the entire fracture method, and (3) the fatigue life expressed in number of cycles to failure N_f, was analysed. The following conclusions can be drawn:

- The strong influence of the low-cycle fatigue strain sequences applied during tests on the fracture surface roughness can be characterised by the core height parameter, Sk;

- Fracture surface parameter Sk calculated using the entire area method in the constant-amplitude and two-step loading tests is linearly dependent on the strain amplitude, ε_a or ε_{aeq}, and logarithmically dependent on the fatigue life, N_f;
- Differences between the values calculated for both parts of the broken sample (side A and side B) as well for the values calculated via the reduced area and the total area were negligible;
- The combination of both the SWT damage parameter and the Miner-Palgren linear damage rule provided accurate fatigue life predictions and can capture the effect of loading sequence under two-step sequences;
- In the Abbott-Firestone plot, the cases with the smallest strain amplitude components for constant-amplitude loading and for the second step of the symmetrical-asymmetrical cases were characterised by the smaller values of height distribution;
- The minimum values of Sk for all cases tested were characterised by a more even histogram distribution and a smaller percentage of depth distribution (about 10%);
- The comparison of the Abbott-Firestone plots for both sides of the fracture surfaces showed a high level of symmetry manifested by a mirror-like image;
- The very similar values of height distribution calculated also confirm that, for the analysis of this type of samples, it does not matter which side of the broken specimen is examined.

Moreover, measurements of fracture surface and their quantitative analysis along with fractography contribute to a better understanding of the fatigue failure process. Regular differences in fatigue fractures were identified, while demonstrating the correctness of the total fracture surface method.

Declaration of competing interest

The author declare that they have no known competing financial interests or personal relationships that could have appeared to influence the work reported in this paper.

Acknowledgments

Appendix A. 3D view, photo simulation, Sk and volume parameters of the extracted area
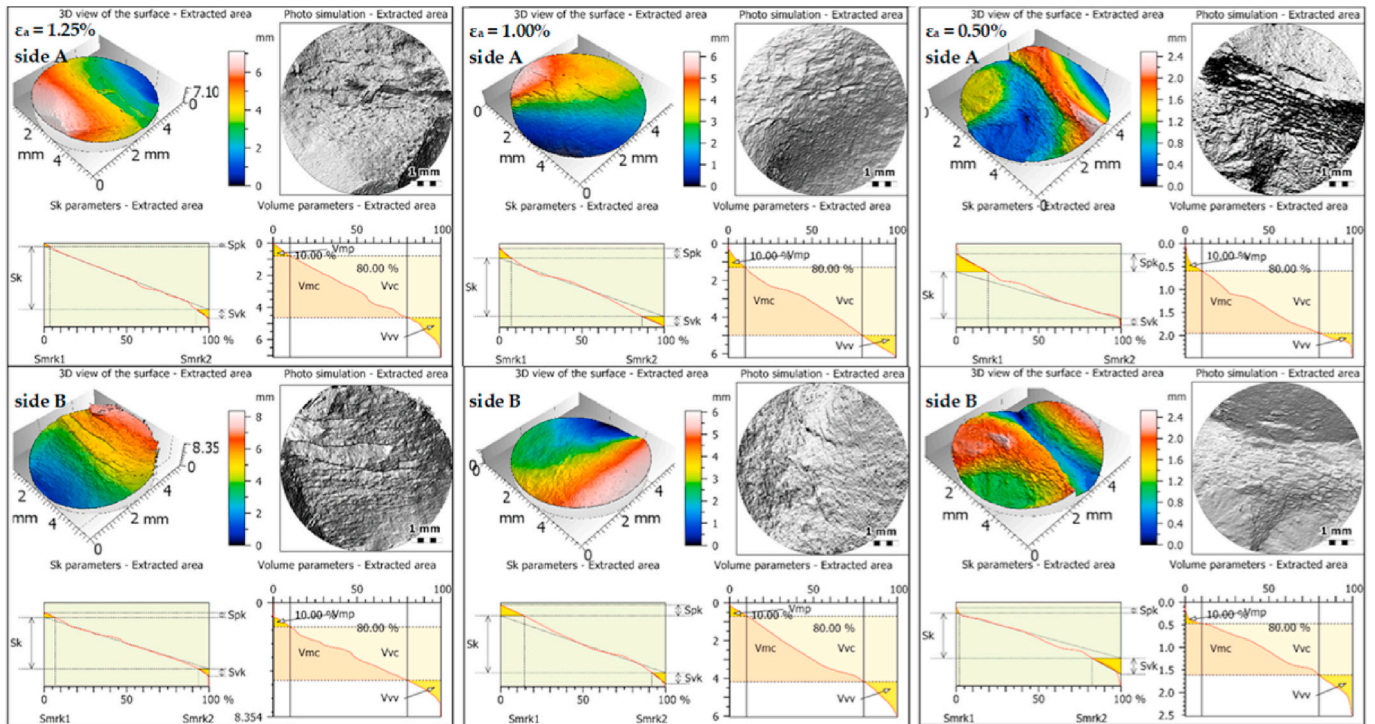
Fig. A1. 3D view, photo simulation, Sk and volume parameters of the extracted area for fractures after constant-amplitude fatigue.
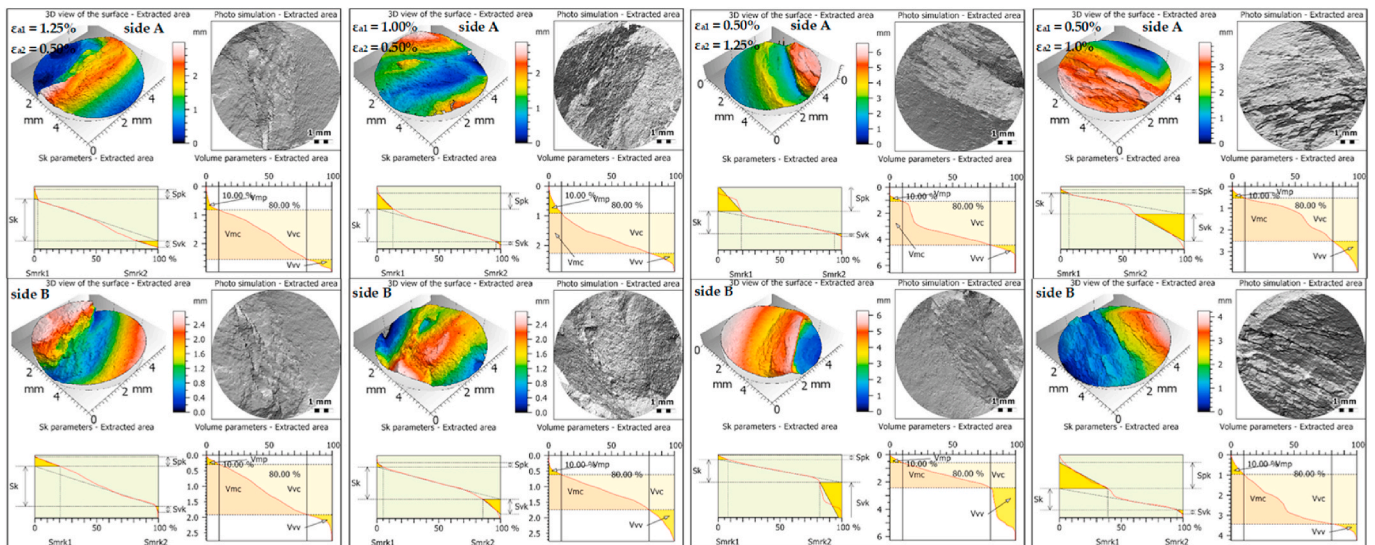

Fig. A2. 3D view, photo simulation, Sk and volume parameters of the extracted area for fractures after two series under different variable amplitude loading conditions with non-zero mean strain values.

Appendix B. Fractured specimen both siedes comparison for photo simulation, 3D view of the extracted, rotated and mirrored areas
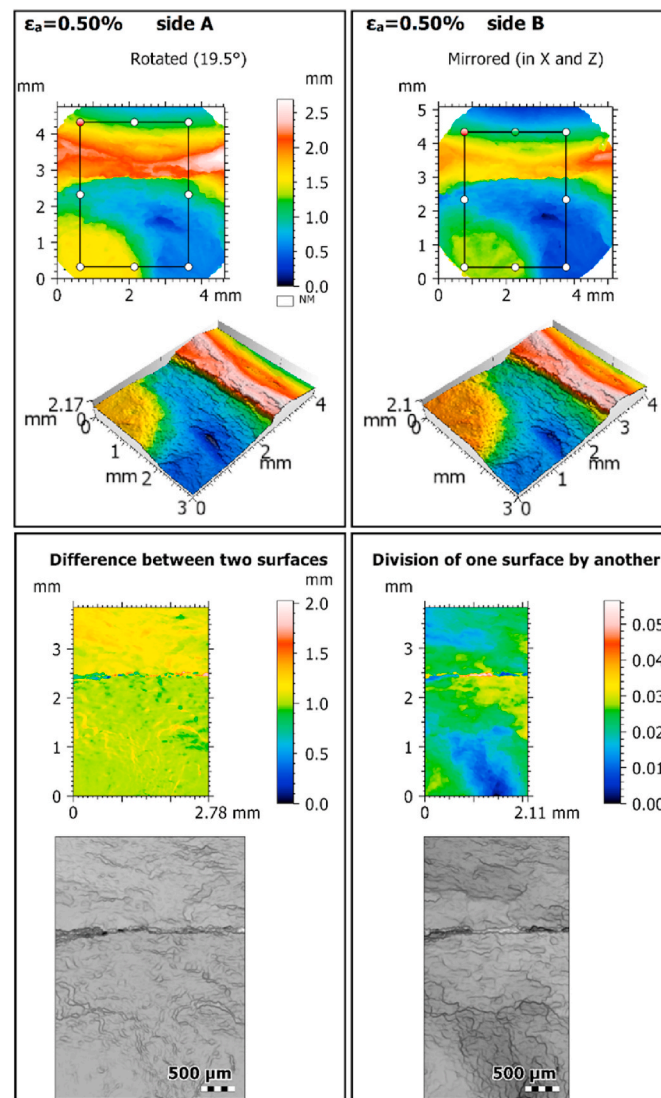
Fig. B1. Examplary specimen comparison (both sides).

References

Baragetti, S., Arcieri, E.V., 2020. Effects of thin hard film deposition on fatigue strength of AA7075-T6. Proc. Inst. Mech. Eng. C J. Mech. Eng. Sci. https://doi.org/10.1177/0954406220980505.

Baragetti, S., Božić, Arcieri, E.V., 2020. Stress and fracture surface analysis of uncoated and coated 7075-T6 specimens under the rotating bending fatigue loading. Eng. Fail. Anal. 112, 104512 https://doi.org/10.1016/j.engfailanal.2020.104512.

Borges, M.F., Antunes, F.V., Prates, P.A., Branco, R., 2020. A numerical study of the effect of isotropic hardening parameters on mode I fatigue crack growth. Metals 10, 177. https://doi.org/10.3390/met10020177.

Branco, R., Costa, J.D., Borrego, L.P., Wu, S.C., Long, X.Y., Zhang, F.C., 2019. Effect of strain ratio on cyclic deformation behaviour of 7050-T6 aluminium alloy. Int. J. Fatig. 129, 105234. https://doi.org/10.1016/j.ijfatigue.2019.105234. ISSN 0142-1123.

Branco, R., Costa, J.D., Martins Ferreira, J.A., Capela, C., Antunes, F.V., Macek, W., 2021. Multiaxial fatigue behaviour of maraging steel produced by selective laser melting. Mater. Des. 201, 109469 https://doi.org/10.1016/j.matdes.2021.109469.

Carpinteri, A., Brighenti, R., Vantadori, S., Viappiani, D., 2008. Static crack extension prediction in aluminium alloy at low temperature. Eng. Fract. Mech. 75, 510–525. https://doi.org/10.1016/j.engfracmech.2007.05.001.

Cisko, A., Jordon, J., Avery, D., Liu, T., Brewer, L., Allison, P., Carino, R., Hammi, Y., Rushing, T., Garcia, L., 2019. Experiments and modeling of fatigue behavior of friction stir welded aluminum lithium alloy. Metals 9, 293. https://doi.org/10.3390/met9030293.

Cunha, J., Mateus, A., Malça, C., Costa, J., Branco, R., 2021. Effect of Strain Load History on Fatigue Behaviour of the 7075-T651 Aluminium Alloy. Springer, Cham, pp. 279–284. https://doi.org/10.1007/978-3-030-35533-3_33.

Fisher, K., Marquis, E., 2016. Comparing plasma-FIB and Ga-FIB preparation of atom probe tomography samples. Microsc. Microanal. 22 (S3), 692–693. https://doi.org/10.1017/S1431927616004311.

Hebda, E., Bukowczan, A., Michałowski, S., Wroński, S., Urbaniak, P., Kaczmarek, M., Hutnik, E., Romaniuk, A., Wolun-Cholewa, M., Pielichowski, K., 2020. Examining the influence of functionalized POSS on the structure and bioactivity of flexible polyurethane foams. Mater. Sci. Eng. C 108, 110370. https://doi.org/10.1016/J.MSEC.2019.110370.

Huang, H., Feng, R., 2006. Dynamic tribological response of SiC fracture surfaces. Mech. Mater. 38, 186–202. https://doi.org/10.1016/j.mechmat.2005.06.009.

ISO - ISO 25178-2, 2012. Geometrical product specifications (GPS) — Surface texture: Areal — Part 2: Terms, definitions and surface texture parameters [WWW Document], n.d. https://www.iso.org/standard/42785.html (accessed 12.28.2020).

Kida, K., Ishida, M., Mizobe, K., Yoshida, I., Tamura, A., Nakane, K., 2017. Fatigue of low carbon alloy steel (JIS S45C) and a new method of fracture surface analysis. Mater. Sci. Forum 893, 181–185. https://doi.org/10.4028/www.scientific.net/msf.893.181.

Kobayashi, T., Shockey, D.A., 2010. Fracture surface topography analysis (FRASTA)— development, accomplishments, and future applications. Eng. Fract. Mech. 77, 2370–2384. https://doi.org/10.1016/J.ENGFRACMECH.2010.05.016.

Lauschmann, H., Šiška, F., 2012. The reference texture: a proposal of a physical explanation. Int. J. Fatig. 43, 120–127. https://doi.org/10.1016/J.IJFATIGUE.2012.03.002.

Macek, W., 2019a. Post-failure fracture surface analysis of notched steel specimens after bending-torsion fatigue. Eng. Fail. Anal. ISSN: 1350-6307 105, 1154–1171. https://doi.org/10.1016/j.engfailanal.2019.07.056.

Macek, W., 2019b. Fractal analysis of the bending-torsion fatigue fracture of aluminium alloy. Eng. Fail. Anal. 99, 97–107. https://doi.org/10.1016/j.engfailanal.2019.02.007.

Macek, Wojciech, Branco, R., Szala, M., Marciniak, Z., Ulewicz, R., Sczygiol, N., Kardasz, P., 2020a. Profile and areal surface parameters for fatigue fracture characterisation. Materials 13, 3691. https://doi.org/10.3390/ma13173691.

Macek, W., Branco, R., Trembacz, J., Costa, J.D., Ferreira, J.A.M., Capela, C., 2020. Effect of multiaxial bending-torsion loading on fracture surface parameters in high-strength steels processed by conventional and additive manufacturing. Eng. Fail. Anal. 118 https://doi.org/10.1016/j.engfailanal.2020.104784.

Macek, W., Marciniak, Z., Branco, R., Rozumek, D., Królczyk, G.M., 2021. A fractographic study exploring the fracture surface topography of S355J2 steel after pseudo-random bending-torsion fatigue tests. Measurement 178, 109443. https://doi.org/10.1016/j.measurement.2021.109443.

Macek, Wojciech, Owsiński, R., Trembacz, J., Branco, R., 2020b. Three-dimensional fractographic analysis of total fracture areas in 6082 aluminium alloy specimens under fatigue bending with controlled damage degree. Mech. Mater. 147 https://doi.org/10.1016/j.mechmat.2020.103410.

Macek, Wojciech, Rozumek, D., Królczyk, G.M., 2020c. Surface topography analysis based on fatigue fractures obtained with bending of the 2017A-T4 alloy. Meas. J. Int. Meas. Confed. 152, 107347 https://doi.org/10.1016/j.measurement.2019.107347.

Madivala, M., Schwedt, A., Prahl, U., Bleck, W., 2019. Strain hardening, damage and fracture behavior of Al-added high Mn TWIP steels. Metals 9, 367. https://doi.org/10.3390/met9030367.

Milner, M.P., Hutchens, S.B., 2021. Multi-crack formation in soft solids during high rate cavity expansion. Mech. Mater. 154, 103741 https://doi.org/10.1016/j.mechmat.2020.103741.

Moutarlier, V., Viennet, R., Gigandet, M.P., Hihn, J.Y., 2020. Use of ultrasound irradiation during acid etching of the 2024 aluminum alloy: effect on corrosion resistance after anodization. Ultrason. Sonochem. 64, 104879 https://doi.org/10.1016/j.ultsonch.2019.104879.

Neves, T., 2019. Cyclic Elasto-Plastic Behavior of 7075-T651 Aluminum Alloy. University of Coimbra, Department of Mechanical Engineering (MSc dissertation thesis [in Portuguese]).

Pandey, V., Singh, J.K., Chattopadhyay, K., Srinivas, N.C.S., Singh, V., 2017. Influence of ultrasonic shot peening on corrosion behavior of 7075 aluminum alloy. J. Alloys Compd. 723, 826–840. https://doi.org/10.1016/j.jallcom.2017.06.310.

Pawliczek, R., Rozumek, D., 2020. The effect of mean load for S355J0 steel with increased strength. Metals 10, 209. https://doi.org/10.3390/met10020209.

Pejkowski, Ł., Skibicki, D., 2019. Stress-strain response and fatigue life of four metallic materials under asynchronous loadings: experimental observations. Int. J. Fatig. 128, 105202 https://doi.org/10.1016/J.IJFATIGUE.2019.105202.

Pomberger, S., Stoschka, M., Aigner, R., Leitner, M., Ehart, R., 2020. Areal fatigue strength assessment of cast aluminium surface layers. Int. J. Fatig. 133, 105423 https://doi.org/10.1016/J.IJFATIGUE.2019.105423.

Ran, J., Fu, M., 2016. Applicability of the uncoupled ductile fracture criteria in micro-scaled plastic deformation. Int. J. Damage Mech. 25, 289–314. https://doi.org/10.1177/1056789515578181.

Rozumek, D., Faszynka, S., 2020. Surface cracks growth in aluminum alloy AW-2017A-T4 under combined loadings. Eng. Fract. Mech. 226, 106896 https://doi.org/10.1016/J.ENGFRACMECH.2020.106896.

Sampath, D., Akid, R., Morana, R., 2018. Estimation of crack initiation stress and local fracture toughness of Ni-alloys 945X (UNS N09946) and 718 (UNS N07718) under hydrogen environment via fracture surface topography analysis. Eng. Fract. Mech. 191, 324–343. https://doi.org/10.1016/j.engfracmech.2017.12.010.

Slámečka, K., Pokluda, J., Kianicová, M., Major, S., Dvořák, I., 2010. Quantitative fractography of fish-eye crack formation under bending-torsion fatigue. Int. J. Fatig. 32 https://doi.org/10.1016/j.ijfatigue.2009.07.009.

Srinivasan, N., Bhaskar, L.K., Kumar, R., Baragetti, S., 2018. Residual stress gradient and relaxation upon fatigue deformation of diamond-like carbon coated aluminum alloy in air and methanol environments. Mater. Des. 160, 303–312. https://doi.org/10.1016/j.matdes.2018.09.022.

Tan, C., Fan, Y., Sun, Q., Zhang, G., 2020. Improvement of the crack propagation resistance in an α + β titanium alloy with a trimodal microstructure. Metals 10, 1058. https://doi.org/10.3390/met10081058.

Todhunter, L.D., Leach, R.K., Lawes, S.D.A., Blateyron, F., 2017. Industrial survey of ISO surface texture parameters. CIRP J. Manuf. Sci. Technol. 19, 84–92. https://doi.org/10.1016/J.CIRPJ.2017.06.001.

Tomczyk, A., Seweryn, A., 2017. Fatigue life of EN AW-2024 alloy accounting for creep pre-deformation at elevated temperature. Int. J. Fatig. 103, 488–507. https://doi.org/10.1016/j.ijfatigue.2017.06.037.

Tsigarida, A., Tsampali, E., Konstantinidis, A.A., Stefanidou, M., 2021. On the use of confocal microscopy for calculating the surface microroughness and the respective hydrophobic properties of marble specimens. J. Build. Eng. 33, 101876 https://doi.org/10.1016/j.jobe.2020.101876.

Vukelic, G., Brnic, J., 2016. Predicted fracture behavior of shaft steels with improved corrosion resistance. Metals 6, 40. https://doi.org/10.3390/met6020040.

Wang, Z., Wu, W., Qian, G., Sun, L., Li, X., Correia, J.A.F.O., 2019. In-situ SEM investigation on fatigue behaviors of additive manufactured Al-Si10-Mg alloy at elevated temperature. Eng. Fract. Mech. 214, 149–163. https://doi.org/10.1016/J.ENGFRACMECH.2019.03.040.

Xu, Z., Han, Y., Fan, C., He, X., Tan, P.J., Huang, F., 2021. Dynamic shear fracture toughness and failure characteristics of Ti–6Al–4V alloy under high loading rates. Mech. Mater. 154, 103718 https://doi.org/10.1016/j.mechmat.2020.103718.

Yu, D., Yang, W., Deng, W., Zhu, S., Dai, Q., Zhang, D., 2021. Crack initiation mechanism in casting AC4B aluminum alloy parts with complex structure. Metals 11, 97. https://doi.org/10.3390/met11010097.

Żebrowski, R., Walczak, M., Korga, A., Iwan, M., Szala, M., 2019. Effect of shot peening on the mechanical properties and cytotoxicity behaviour of titanium implants produced by 3D printing Technology. J. Healthc. Eng. 2019, 11. https://doi.org/10.1155/2019/8169538, 8169538.

Zhang, S., Lu, Y., Shen, Z., Zhou, C., Lou, Y., 2020. Prediction of ductile fracture for Al6016-T4 with a ductile fracture criterion: experiment and simulation. Int. J. Damage Mech. 29, 1199–1221. https://doi.org/10.1177/1056789519865771.